ADVANCING EARTH AND SPACE SCIENCES

JGR Space Physics

RESEARCH ARTICLE

10.1029/2024JA032558

Key Points:

- A global hybrid simulation to understand the suprathermal outflowing H^+ ions observed in southern lobe driven by an interplanetary shock
- The simulated outflowing H^+ ions in the lobe are outflows from the polar cap driven by enhanced Poynting fluxes caused by the shock impact
- The simulated outflowing H^+ ions can account for the observed pitch-angle distribution and the time delay from the shock impact

Supporting Information:

Supporting Information may be found in the online version of this article.

Correspondence to:

C.-P. Wang,
cat@atmos.ucla.edu

Citation:

Wang, C.-P., Wang, X., Lin, Y., Mouikis, C. G., & Masson, A. (2024). Suprathermal outflowing H^+ ions in the lobe driven by an interplanetary shock: 2. A 3D global hybrid simulation. *Journal of Geophysical Research: Space Physics*, *129*, e2024JA032558. https://doi.org/10.1029/2024JA032558

Received 16 FEB 2024
Accepted 31 AUG 2024

Suprathermal Outflowing H^+ Ions in the Lobe Driven by an Interplanetary Shock: 2. A 3D Global Hybrid Simulation

Chih-Ping Wang[1], **Xueyi Wang**[2], **Yu Lin**[2], **C. G. Mouikis**[3], **and Arnaud Masson**[4]

[1]Department of Atmospheric and Oceanic Sciences, University of California, Los Angeles, CA, USA, [2]Physics Department, Auburn University, Auburn, AL, USA, [3]Space Science Center, University of New Hampshire, Durham, NH, USA, [4]European Space Agency, European Space Astronomy Center, Madrid, Spain

Abstract We conduct a global hybrid simulation of an observation event to affirm that an interplanetary (IP) shock can drive significant suprathermal (tens to hundreds of eV) H^+ outflows from the polar cap. The event showed that a spacecraft in the lobe at ∼6.5 R_E altitude above the polar cap observed the appearance of suprathermal outflowing H^+ ions about 8 min after observing enhanced downward DC Poynting fluxes caused by the shock impact. The simulation includes H^+ ions from both the solar wind and the ionospheric sources. The cusp/mantle region can be accessed by ions from both sources, but only the outflow ions can get into the lobe. Despite that upward flowing solar wind ions can be seen within part of the cusp/mantle region and their locations undergo large transient changes in response to the magnetosphere compression caused by the shock impact, the simulation rules out the possibility that the observed outflowing H^+ ions was due to the spacecraft encountering the moving cusp/mantle. On the other hand, the enhanced downward DC Poynting fluxes caused by the shock impact drive more upward suprathermal outflows, which reach higher altitudes a few minutes later, explaining the observed time delay. Also, these simulated outflowing ions become highly field-aligned in the upward direction at high altitudes, consistent with the observed energy and pitch-angle distributions. This simulation-observation comparison study provides us the physical understanding of the suprathermal outflow H^+ ions coming up from the polar cap.

1. Introduction

The H^+ ions in the magnetosphere can come from two sources: the solar wind source and the ionospheric source. Ions from the ionospheric source (ionosphere outflows) can flow into different magnetosphere regions, including the cusp, mantle, and lobe at high latitudes within the open field-line region and the plasma sheet and plasmasphere at lower latitudes within the closed field-line region magnetosphere (e.g., Chappell et al., 1987, 2000). The ion outflows can be separated into two categories (e.g., Yau et al., 2011): (a) "bulk ion flows" are thermal outflows with energies up to a few eV, such as the polar wind, and (b) "suprathermal ion outflows" are more energetic outflows with energies from tens to hundreds of eV, such as ion beams and ion conics. The outflow fluxes have been found to correlate with several outflow drivers from the magnetosphere (e.g., Strangeway et al., 2005; Zhao et al., 2020), including downward DC Poynting flux (note that downward is toward the ionosphere in this paper), downward AC Poynting flux, electric field amplitude of extremely low-frequency waves, precipitating electron density, precipitating electron number flux, and precipitating electron energy flux. These magnetospheric drivers are affected by the coupling of the magnetosphere with the solar wind as well as the disturbances within the magnetosphere.

Above the polar cap, suprathermal H^+ outflows are much less frequently observed, as compared to the polar wind (e.g., Peterson et al., 2008). As presented in a companion paper (Wang, Mouikis, et al., 2024; hereafter referred to as Paper 1), we reported an event that indicated that an interplanetary (IP) shock can drive a significant amount of suprathermal H^+ outflows from the polar cap. During the IP shock event, a Cluster spacecraft in the southern lobe at altitudes of ∼6 R_E observed suprathermal outflowing H^+ ions that appeared about 8 min after observing enhanced downward DC Poynting fluxed driven by the impact of the IP shock. Based on the comparisons with the cusp ions simultaneously observed by another Cluster spacecraft, we concluded that it is less likely that these outflowing ions in the lobe were due to the encounter with the moving cusp as a result of the magnetosphere compression by the shock impact. The observed outflowing ions in the lobe had particle distributions of ion beams and ion conics, strongly suggesting that they were outflows coming from the polar cap. To evaluate whether these observations can indeed be accounted for by processes resulting from the impact of an IP shock, in this study we use a three-dimensional (3D) global hybrid code to simulate the distributions of the H^+ ions from both the solar wind and ionospheric sources and investigate their changes in response to the shock impact. The hybrid simulation can predict ion energy and pitch-angle distributions, which plays a crucial role in our simulation-observation comparisons. Our simulation results support the conclusion that the observed suprathermal outflowing H^+ ions in the lobe were contributed by enhanced outflows coming from the polar-cap region driven by enhanced downward DC Poynting fluxes caused by the shock impact. We describe the model and simulation setup in Section 2. The simulation results are presented in Section 3 and compared with the observation results from Paper 1. Conclusions and discussion are given in Section 4.

2. Model and Simulation Description

We use the 3D global hybrid code, AuburN Global hybrId CodE in 3D (ANGIE3D), to simulate the ion dynamics. Details of the equations for ion particle motion, electric and magnetic fields, and assumptions used in the ANGIE3D code are described in Lin et al. (2014). The ions are treated as discrete, fully kinetic particles, and the electrons are treated as a massless fluid, while a cold, plasmaspheric ion fluid in $r < 6\ R_E$ is also imposed. Quasi charge neutrality is assumed. The code is valid for low-frequency physics with $\omega \sim \Omega_i$ and $k\rho_i \sim 1$ (wavelength $\lambda \sim 6\rho i$), where ω is the wave frequency, k is the wave number, Ω_i is the ion gyrofrequency, and ρ_i is the ion Larmor radius (gyroradius). ANGIE3D has been used to simulate the impact of an IMF discontinuity on the magnetosphere configuration (Lin et al., 2022; Wang et al., 2020, 2021a, 2021b, 2022) as well as on the ionosphere outflow ions (Wang et al., 2023).

For this study, the simulation domain is $20 \geq X \geq -60$, $32 \geq Y \geq -32$, $32 \geq Z \geq -32\ R_E$ in the geocentric solar magnetospheric (GSM) coordinates. An inner boundary is assumed at the geocentric distance of $r \approx 3\ R_E$. The solar wind ion inertial length d_{i0} in this simulation is 0.06 R_E. Note that this d_{i0} value is three times the realistic value. Thus, scaling factors are used when converting the simulation results to realistic magnitudes (Lin et al., 2014; Omidi et al., 2006). Nonuniform cell grids are used, with the grid size (~0.1–0.15 R_E) around the bow shock, magnetosheath, magnetopause, cusp, and equator smaller than in other places. The cell dimensions are $n_x \times n_y \times n_z = 839 \times 500 \times 768$. A total of $\sim 10^{12}$ particles are used. Uniform Pedersen conductance of 10 S and Hall conductance of 5 S are specified for solving the electric field potential in the ionosphere.

In this simulation, we consider only H^+ ions (i.e., no heavy ions are included). We include the ions from two sources: the solar wind source and the ionospheric source. It is important to note that the ionospheric outflows driven by the energy sources coming down from the magnetosphere involve complicated magnetosphere-ionosphere-thermosphere coupling processes occurring in the ionosphere/thermosphere for generating the cold polar wind ions as well as acceleration processes from topside ionosphere to ~2 R_E altitude to accelerate polar winds to suprathermal ion beams and ion conics (see also Discussion Section of Paper 1). Currently, the global codes cannot directly model these complicated physical processes below ~3 R_E altitude so the outflows in the global simulations can only be included by either specifying them based on the empirical values and empirical correlations with the magnetospheric energy sources established from observations or by coupling with the ionosphere/thermosphere modeling. To include the outflow ions in ANGIE3D, we adapt the algorithm of Brambles et al. (2010). The outflow ions are specified with four parameters at $r = 2\ R_E$: particle flux ($\mathrm{Flux}_{\mathrm{outflow}}$), parallel bulk flow speed ($V_{\parallel,\mathrm{outflow}}$), and parallel temperature ($T_{\parallel,\mathrm{outflow}}$) and perpendicular temperature ($T_{\perp,\mathrm{outflow}}$). The $\mathrm{Flux}_{\mathrm{outflow}}$ affects the outflow ion density while $V_{\parallel,\mathrm{outflow}}$, $T_{\parallel,\mathrm{outflow}}$, and $T_{\perp,\mathrm{outflow}}$ affect the energy of the outflows as well as whether and when the outflow ions can reach certain locations in the magnetosphere. There are empirical formulas available for specifying $\mathrm{Flux}_{\mathrm{outflow}}$. In this study we use the empirical formula of Zhao et al. (2020) established statistically from FAST observations in the cusp, $\mathrm{Flux}_{\mathrm{outflow}} = 1.832 \times 10^5 {S_{\mathrm{DC},\parallel}}^{1.127}$, where the flux is in units of 1/(cm^2-s) and $S_{\mathrm{DC},\parallel}$ is the downward field-aligned DC Poynting flux in mW/m^2. The values of $\mathrm{Flux}_{\mathrm{outflow}}$ change self-consistently and simultaneously with the simulated $S_{\mathrm{DC},\parallel}$. However, there are no empirical formulas available for specifying $V_{\parallel,\mathrm{outflow}}$, $T_{\parallel,\mathrm{outflow}}$, and $T_{\perp,\mathrm{outflow}}$. Since the purpose of this simulation is to help understand the observed enhancement of suprathermal outflows at high altitudes with a time delay from the enhancement of $S_{\mathrm{DC},\parallel}$ reported in Paper 1, we want to specify values for $V_{\parallel,\mathrm{outflow}}$, $T_{\parallel,\mathrm{outflow}}$, and $T_{\perp,\mathrm{outflow}}$ so that corresponding outflow H^+ ions can reasonably represent upgoing suprathermal ion beams and ion conics with energies similar to those observed and they can reach high-latitude lobe locations with a travel time comparable to the observed time delay. To find reasonable values we conduct several test runs using values for $V_{\parallel,\mathrm{outflow}}$, $T_{\parallel,\mathrm{outflow}}$, and $T_{\perp,\mathrm{outflow}}$ within different ranges (with an order of magnitude difference between the ranges), compare the resulting outflow spatial distributions and energies between runs, and present in this paper the run whose results are within the observed ranges. The values used in this run are $V_{\parallel,\mathrm{outflow}} = 40$ km/s, $T_{\parallel,\mathrm{outflow}} = T_{\perp,\mathrm{outflow}} = 100$ eV. It is important to note that we do not restrict the outflow to only the cusp region as in Brambles et al. (2010), and thus outflow can also come from other regions, including the polar cap and auroral zone (Wang et al., 2023). As shown in Section 3, the outflows from the polar cap are essential for this simulation to be able to account for the observations presented in Paper 1. We also use an M-I coupling module to handle the mapping of these parameter values along the dipole magnetic field line between the different altitudes from the ionosphere-thermosphere model at $r \sim 1\ R_E$ to the inner boundary surface at $r = 3\ R_E$. For example, the mapping of $\mathrm{Flux}_{\mathrm{outflow}}$ is determined by conserving $\mathrm{Flux}_{\mathrm{outflow}}/B_{\mathrm{dip}}$, where B_{dip} is the dipole magnetic field strength. In this study, we consider no dipole tilt.

We conduct a simulation of the magnetosphere in response to an IP shock with the solar wind parameters and IMF similar to those observed in the IP shock event presented in Paper 1. A planar discontinuity (a thickness of 0.5 R_E and the normal direction of (1, 0, 0)) with a shock jump condition is used to specify the changes of the IMF and plasma moments associated with the IP shock. Figure 1 shows the specified IMF and solar wind parameters arriving at a location in front of the bow shock at $X = 15$, $Y = 0$, and $Z = -14\ R_E$. The front of the IP shock arrives at this location at $t \sim 30$ min. Associated with the shock, Figure 1e shows that the solar wind dynamic pressure (P_{SW}) jumps sharply by a factor of ∼4.6 from ∼1.5 to 7 nPa and stays at 7 nPa for about 8 min before returning to 1.5 nPa. For the P_{SW} increase seen at $t \sim 30$ min, the IMF B_z becomes more negative while the IMF B_x and IMF B_y do not change (Figure 1a), the IMF magnitude increases by a factor of 3 (Figure 1b), the solar wind density increases by a factor of 3 (Figure 1c), the solar wind speed increases slightly by a factor of 1.2 (Figure 1d), and the solar wind electric field increases by a factor of 4 (Figure 1e). The corresponding Mach number decreases from ∼7 to 4. These specified changes are similar to the observed changes shown in Figure 1 of Paper 1. In this paper, all the plasma quantities (e.g., particle flux, density, temperature, thermal pressure, and bulk flow) associated with the H^+ ions from the solar wind source only are indicated by the subscript "Sun", those associated with the H^+ ions from the ionospheric source only are indicated by the subscript of "Out", and those including both sources are indicated by the subscript of "Tot."

3. Simulation Results

In this section, we present the response of magnetic fields and H^+ ions to the impact of the IP shock in the cusp and lobe, evaluate separately the ions from the solar wind and ionosphere, and compare the simulation results with the observations of Paper 1.

3.1. Overview

The X–Z distributions of the number densities of the H^+ ions from each of the two sources at $Y = 0$ from $t = 27$ to 41 min are shown in Movie S1, together with temperatures for ions from each source, the bulk flows combining the two sources, magnetic fields, and electric fields, and downward Poynting fluxes. Note that, in this paper, the contour of $N_{\mathrm{Sun}} = 5\ \mathrm{cm}^{-3}$ is used to indicate approximately the boundaries of the magnetopause and the cusp. The P_{SW} jump pushes the magnetopause inward, causes changes in magnetospheric magnetic fields, moves the exterior cusp to lower altitudes, enhances magnetospheric convection, enhances downward DC Poynting fluxes propagating inward and tailward from the magnetopause, and the enhanced Poynting fluxes reaching the model's inner boundary drives more outflow H^+ ions flowing outward into the cusp and the lobe.

We show in Figure 2 an overview of the simulation results in a way for comparisons with the overview of the observational event presented in Figure 2 of Paper 1. The IP shock arrives at the magnetosheath just outside the southern cusp at $t \sim 31.5$ min Figure 2a shows the X–Z distributions of N_{Tot} (densities including both sources) at three different times: before the shock impact ($t = 28$ min), during the impact on the dayside magnetosphere ($t = 35$ min), and after the impact ($t = 41$ min). As indicated by the gray contours of $N_{\mathrm{Sun}} = 5\ \mathrm{cm}^{-3}$, the magnetopause is first pushed inward during the impact and then moves outward after the impact. The cusp region moves toward the dayside in response to the impact. To compare with the observations of the two Cluster spacecraft (C1 and C3) in Paper 1, we select two locations for two virtual spacecraft: Location 1 ($X = 2.5$, $Y = 0$, $Z = -5.8\ R_E$, indicated by the triangle in Figure 2a) is at the very vicinity of the cusp, similar to C1. Location 2 ($X = -1$, $Y = 0$, $Z = -6.8\ R_E$, indicated by the circle in Figure 2a) is in the lobe, similar to C3. Note that, unlike Cluster spacecraft, the two virtual spacecraft locations are fixed during the impact. We also map locations 1 and 2

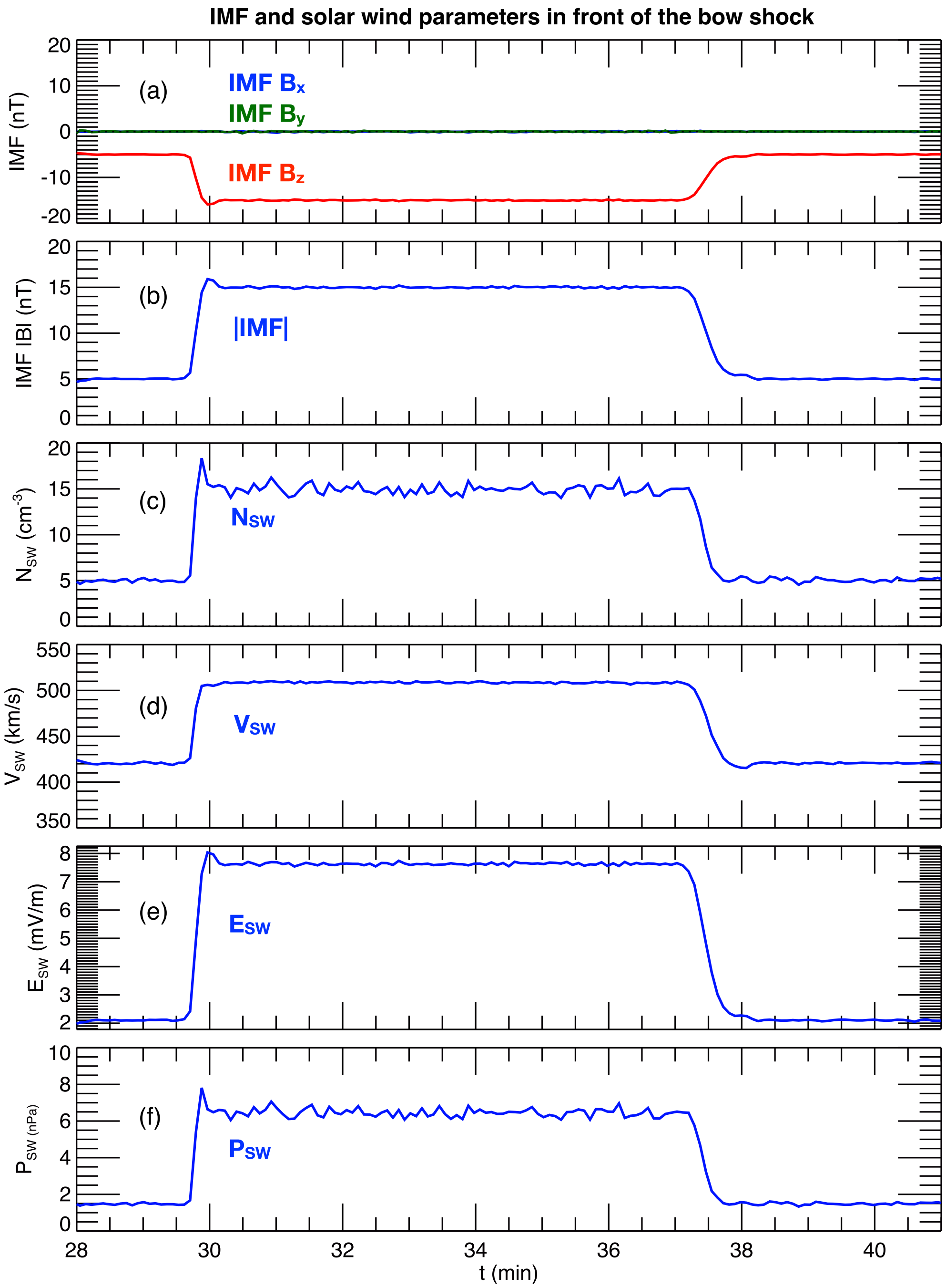

Figure 1. The IMF and solar wind conditions for the IP shock at a location in front of the bow shock ($X = 15$, $Y = 0$, $Z = 13\ R_E$). (a) IMF components, (b) IMF magnitudes, (c) solar wind number densities, (d) solar wind flow speeds, (e) solar wind electric field, and (f) solar wind dynamic pressures.

to low altitudes at $r = 3.1\ R_E$ just outside the model's inner boundary (the green lines in the $t = 28$ min indicate magnetic field lines): location 3 is the footprint of location 1 and located within the cusp while location 4 is the footprint of location 2 and located within the polar cap. Figures 2b–2e show the temporal profiles at location 1 (left panels) and location 2 (right panels) for magnetic field components, magnetic field strength, N_{Tot} and N_{Out}, and the omnidirectional energy fluxes for H^+ ions from both sources. Figures 2f and 2g show the temporal profiles of Poynting fluxes and N_{Out} at location 3 (left panels) and location 4 (right panels). For the magnetic fields, in response to the shock impact, at t ~32 min at location 1 (indicated by the vertical dotted line in the left panel of

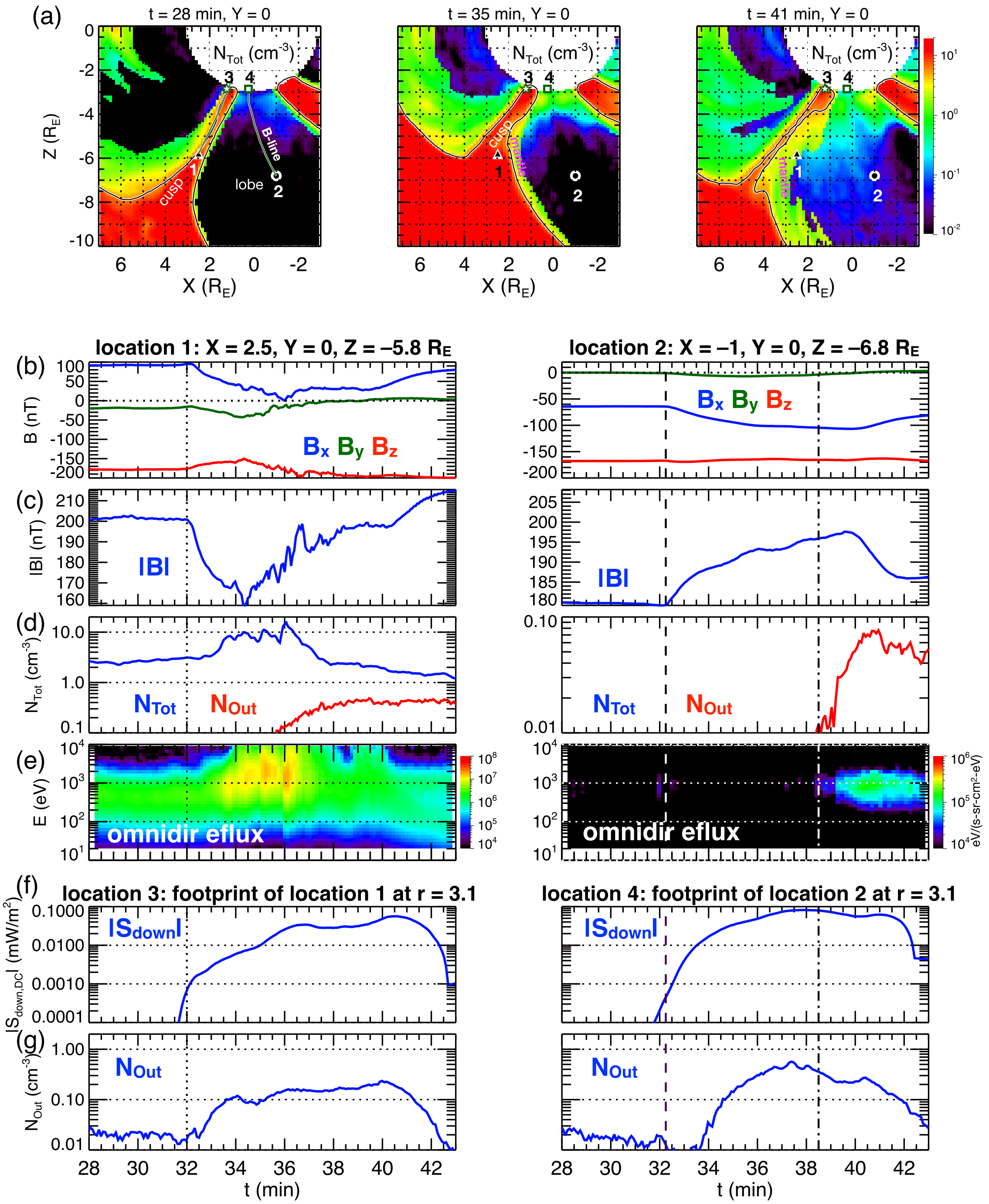

Figure 2. (a) X–Z profiles (at $Y = 0$) of the N_{Tot} (the density including both H^+ particles from the solar wind and the ionosphere) for $t = 28$, 35, and 41 min. The triangle and circle indicate location 1 and 2, respectively. The green lines in $t = 28$ plot indicate magnetic field lines and location 3 (star) and 4 (square) are the footprints of location 1 and 2, respectively, at $r = 3.1\ R_E$. The gray curve is the contour of $N_{\mathrm{Tot}} = 5\ \mathrm{cm}^{-3}$ used to indicate approximately the cusp and magnetopause on the dayside. The regions of "cusp", "mantle", and "lobe" are indicated. Temporal profiles of (b) the three magnetic field components, (c) magnetic field strength, (d) N_{Tot} and N_{Out}, and (e) energy spectrum of omnidirectional energy fluxes for H^+ ions from both the solar wind and ionosphere at location 1 (left panels) and location 2 (right panels). Temporal profiles of (f) Poynting fluxes and (g) outflow H^+ density at location 3 (left) and 4 (right).

Figure 2) the B_x component decreases from positive values to almost zero and the B_z component becomes less negative (Figures 2b and 2c), while the magnetic field strength decreases (Figure 2c). About 15 s later at location 2 (indicated by the dashed vertical line in the right panels), the B_x component becomes more negative and the B_z

component becomes less negative, while the magnetic field strength increases. At both locations, the changes in the B_y component are much smaller than the changes in other components. These simulated magnetic field changes and the very short delay between the two locations are qualitatively similar to the observed changes shown in Figures 2d and 2e of Paper 1. More details about the simulated magnetic fields are presented in Section 3.2. At approximately the same time as the sharp magnetic field changes at locations 1 and 2, at their footprint locations 3 and 4 downward Poynting fluxes increased sharply (Figure 2f), resulting in sharp increases in the outflow H^+ density ~1 min later. For the H^+ ions, in the cusp at location 1, the density (Figure 2d) and particle fluxes (Figure 2e) increase significantly ~1 min after the magnetic field changes and these ion increases correspond to the decrease in magnetic field strength. But outflow H^+ density at location 1 only starts to increase about 3 min after the increase seen at its footprint location 3. On the other hand, only outflow H^+ ions are seen in the lobe at location 2 (note that N_{Tot} in the right panel of Figure 2d is the same as N_{Out}) and they only start to appear at t ~38.5 min (indicated by the vertical dotted-dashed line in the right panels), which is ~6 min after the magnetic field changes and ~5 min after the outflow density increase seen in its footprint location 4. These simulated changes in the H^+ ions and their correspondence to the magnetic field changes at locations 1 and 2, in particular the time delay seen in the lobe, are similar to the observed H^+ ions shown in Figures 2f and 2g of Paper 1. We further investigate these simulated H^+ changes in the cusp region in Section 3.3 and in the lobe region in Section 3.4 with a focus on the pitch-angle distributions for ions from each of the two sources.

3.2. Magnetic Field Changes Due To the IP Shock

We investigate in Figure 3 the shock impact on the magnetic field changes for B_x (Figure 3a), B_y (Figure 3b), B_z (Figure 3c), and $|B|$ (Figure 3d). The fields before the impact at $t = 28$ min, during the impact at $t = 35$ min, and the differences (subtract the fields of $t = 28$ min from the fields of $t = 35$ min) are shown in the left, middle, and right panels, respectively.

The right panels of Figures 3a–3c show that, for most of the higher-altitude region (above ~4 R_E altitudes) from the cusp to the lobe, the impact causes a negative change in B_x and B_y (the right panels of Figures 3a and 3b.). For the B_z component, a positive change is seen in the cusp (the right panel of Figure 3c). But in the lobe, the B_z change switches from being positive to negative with increasing altitudes. The magnetic field strength shows a negative change in the cusp (the right panel of Figure 3d), while the $|B|$ change in the lobe switches from being negative to positive with increasing altitudes. In general, the spatial distributions of the simulated changes in B_x, B_z, and $|B|$ are qualitatively similar to those of the empirical T96 fields (Figure 3 of Paper 1). There are clear differences in the B_y component between the simulation and the T96 fields, likely due to that IMF B_y is set to be zero in the simulation.

As shown in Figure 3e, the simulated B_y in the lobe at location 2 shows a bipolar perturbation with a positive perturbation first ($\delta B_y = B_y - \langle B_y \rangle$, where $\langle B_y \rangle$ is the 6-min running average) after the impact, which is similar to the bipolar perturbation observed by spacecraft C3 in the lobe shown in the right panel of Figure 3f in Paper 1. In the simulation, the bipolar B_y perturbation corresponds to a transient enhancement in the upward field-aligned current ($J_{\|}$) in the lobe (Figure 3f) as the IP shock causes enhanced upward $J_{\|}$ propagating tailward in the lobe (comparing the X–Z distributions of $J_{\|}$ between $t = 28$ and 33 min shown in Figure 3g).

3.3. Changes in the Cusp Structure and H^+ Distributions Due To the IP Shock

To better understand the C1 observations in the cusp during the shock impact presented in Paper 1, we focus, in this section, on the simulation results at location 1. Figure 4 shows the spatial distributions of the plasma quantities around the cusp for the H^+ ions including both the solar wind and ionospheric sources. The X–Z distributions of N and $V_{\|}$ are shown in Figures 4a and 4b, respectively, for three different times (t = 28.1, 33.3, and 40.2 min), and the cross-cusp profiles (along the fixed dashed line in Figures 4a and 4b) at these times are shown in Figures 4c–4i. At all times, the cusp is wider at higher altitudes closer to the magnetopause (Figure 4a). Before the shock impact, as seen in the cross-cusp profiles at $t = 28$ min (blue lines in Figures 4c–4i), at the center of the cusp (X ~2.7 R_E) the relatively higher density (up to ~15 cm^{-3}, Figure 4c) and temperature (up to ~800 eV, Figure 4d) result in higher thermal pressure (up to ~ 2 nPa, Figure 4e) and lower magnetic field strength (Figure 4f) and magnetic pressure (Figure 4g), as compared to the values at the edge of the cusp (X ~2.1 R_E). This magnetic depression is the diamagnetic signature of the cusp. Such depression is more significant in the portion of the cusp closer to the magnetopause termed "the exterior cusp." Shortly after the impact, as seen

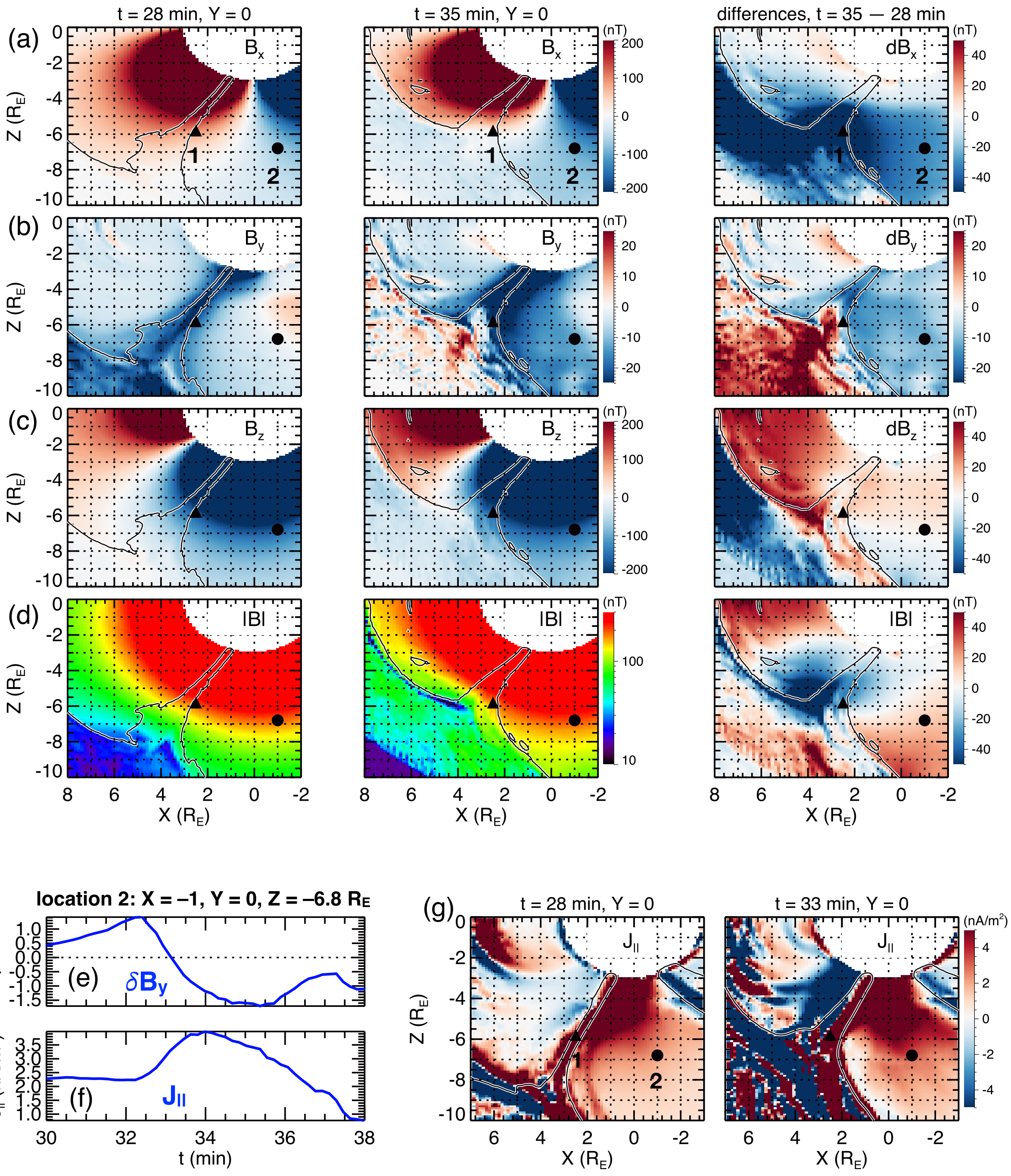

Figure 3. (a–d) X–Z profiles (at $Y = 0$) of the ANGIE3D magnetic fields in (a) B_x, (b) B_y, (c) B_z, and (d) |B| for $t = 28$ min before the P_{SW} jump (left panels) and for $t = 35$ min after the P_{SW} jump (middle panels), and the differences (the fields of $t = 35$ min–the fields of $t = 28$ min). The locations 1 and 2 are indicated by the black triangle and black circle, respectively, in (a). The temporal profiles of (e) δB_y (the perturbations from 6-min B_y running averages) and (f) field-aligned currents ($J_{\parallel}$) at location 2. (g) X–Z profiles of $J_{\parallel}$ at $t = 28$ and 33 min.

in the plots at $t = 33.3$ min, the exterior cusp moves to lower altitudes. As a result, the cross-cusp profiles at $t = 33.3$ min (red lines in Figures 4c–4i) show a wider cusp with more significant magnetic depression, as compared to the profiles at $t = 28.1$ min. After the IP shock passes the Earth, as seen in the plots at $t = 40.2$ min, the magnetopause and the exterior cusp are moving outward so that the dashed line in Figures 4a and 4b at the time cuts through the portion of the cusp at relatively lower altitudes. The direction of the parallel flow across the cusp changes in response to the shock impact. At the altitudes of the dashed line, Figure 4h shows that $V_{\parallel}$ is mainly

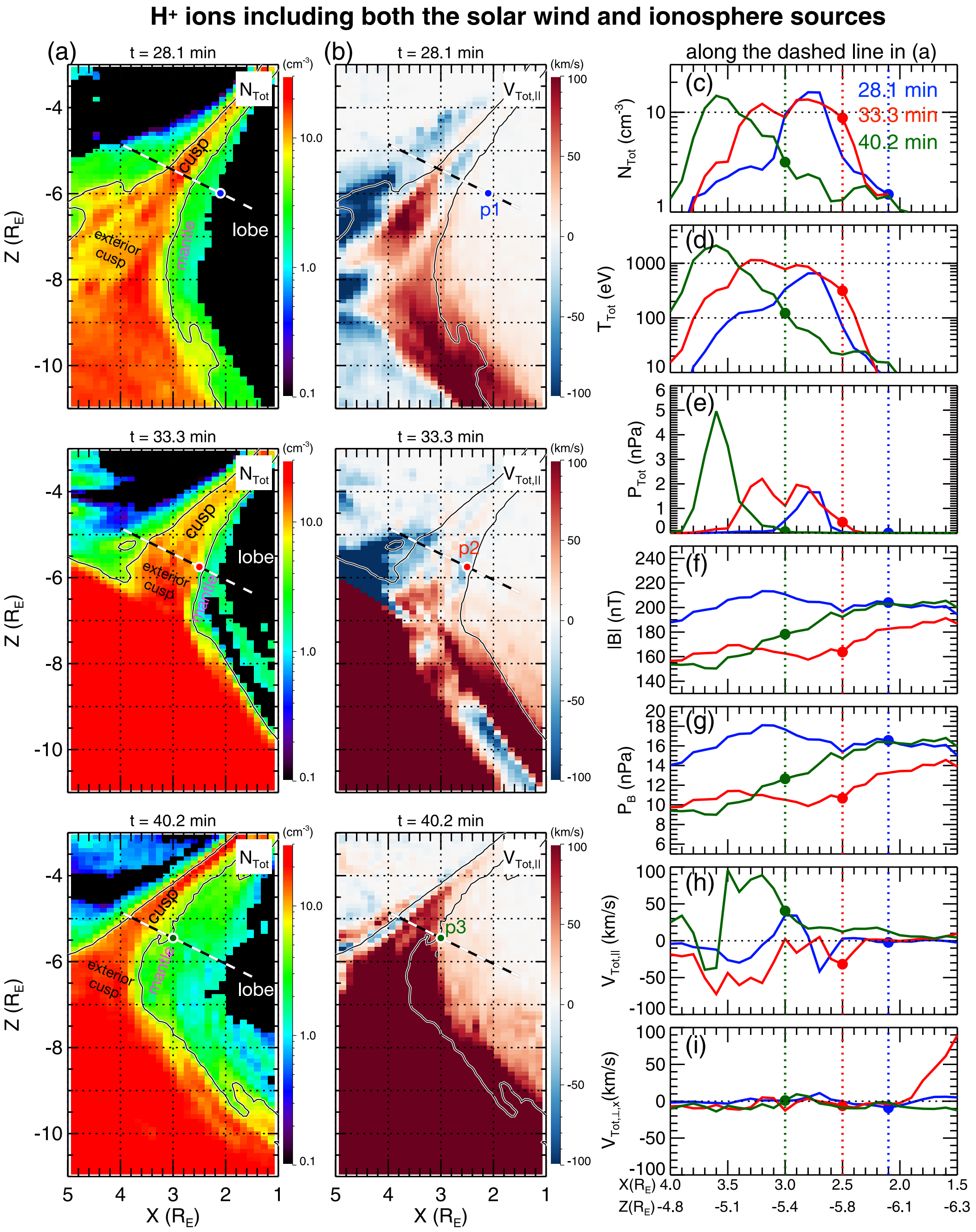

Figure 4. The X–Z profiles (at $Y = 0$) of the ANGIE3D (a) density and (b) parallel velocity of the H^+ ions from both the solar wind and ionosphere at $t = 28.1$ (top), 33.3 (middle), and 40.2 min (bottom) (c–i) The spatial profiles across the cusp along the dashed line in (a) for (c) density, (d) temperature, (e) plasma thermal pressure, (f) magnetic field strength, (g) magnetic pressure, (h) the parallel velocity, and (i) the perpendicular velocity in the X direction at $t = 28.1$ (blue), 33.3 (red), and 40.2 min (green). The locations of the blue (p1), red (p2), and green (p3) dots in (c–i) are indicated in (a, b) for $t = 28.1$, 33.3, and 40.2 min plots, respectively.

downward near the side of the plasma sheet and upward near the side of the lobe before the impact. $V_{\parallel}$ becomes mainly downward within the cusp during the impact but turns upward after the impact. In comparison, Figure 4i shows that the $V_{\perp x}$ speed across the cusp remains small at all times.

In Paper 1, spacecraft C1 was in the cusp during the shock impact and it encountered first the exterior cusp (purple shaded interval) followed by upward-flow-dominated cusp/mantle region. The observed changes included both the spatial variations as measured by the moving spacecraft as well as the temporal variations of the cusp in response to the changing P_{SW}. Thus, for comparison, we choose in Figure 4 of this paper three locations ($p1$, $p2$, and $p3$), each location at one of the three different times along the dashed line shown in Figure 4a: $p1$ is at $X = 2.1$ and $Z = -6.0\ R_E$ at $t = 28.1$ min (blue dot) for comparing with the observation in the vicinity of the cusp before the impact, $p2$ is at $X = 2.5$, $Z = -5.75\ R_E$ at $t = 33.3$ min (red dot) for comparing with the observed exterior cusp, and $p3$ is at $X = 3$, $Z = -5.45\ R_E$ at $t = 40.2$ min (green dot) for comparing with the upward-flow-dominated cusp/mantle transition region. The simulated density changes from ~1 ($p1$), to 10 ($p2$), then to 3 cm^{-3} ($p3$) (Figure 4c), the temperature changes from ~10 ($p1$), to 500 ($p2$), then to 100 eV ($p3$) (Figure 4d), the thermal pressure changes from ~0.1 ($p1$), to 0.5 ($p2$), then to 0.1 nPa ($p3$) (Figure 4e), the magnetic pressure changes from 16 ($p1$), to 10 ($p2$), then 12 nPa ($p3$) (Figure 4g), and the parallel speed changes from ~0 ($p1$) to −50 ($p2$), then to 50 km/s ($p3$) (Figure 4h). These simulated changes are qualitatively consistent with the C1 observations (Figures 4a–4d of Paper 1), explaining that the observed large changes in the plasma moments and magnetic fields were a result of the exterior cusp being pushed to the spacecraft location by the magnetosphere compression in response to the large and sharp P_{SW} jump.

We now investigate separately the H^+ ions from the two sources. Figures 5a and 5b show the time sequence of the X–Z distributions of density for the H^+ ions from the solar wind and ionosphere, respectively. The ions from the solar wind have access to location 1 around the cusp (black triangle in Figure 5a) but not to location 2 in the lobe (black circle in Figure 5a). These solar wind ions reach location 1 either through coming downward from the magnetosheath or, after being mirrored back at lower altitudes, coming upward from below. Those who are mirrored back up contribute to the mantle plasma seen just tailward of the cusp and just inside the high-latitude magnetopause. In comparison, the outflow ions, coming out from both within the cusp ionosphere and the polar cap, are able to reach both locations 1 and 2 (Figure 5b). For the outflow ions, their density starts to increase at the model inner boundary at $r = 3\ R_E$ (comparing the plots between $t = 32.2$ and 33.1 min) due to enhanced downward Poynting fluxes driven by the shock impact and it takes a few minutes for the enhanced density to move upward to locations 1 and 2. As shown in Figures 6a and 6b for the trajectories of the outflow H^+ ions that pass through locations 1 and 2, respectively, at $t = 39$ min, the H^+ outflows reaching location 1 come from the cusp and those reaching location 2 are from the polar cap.

We compare in Figure 7 the H^+ energy spectrum at different pitch angles from the two sources at location 1 around the cusp. As shown in Figures 7a and 7b for the solar wind ions, they are seen at all pitch angles and the fluxes are relatively higher in the perpendicular direction than the two field-aligned directions. This anisotropy remains approximately so even when the distribution is shifted slightly toward the upward direction after $V_{||}$ at location 1 becomes substantially upward after $t \sim 37$ min (see Movie S1) as location 1 is getting closer to the cusp/mantle transition region. This pitch-angle distribution for the solar wind ions is qualitatively similar to the Cluster C1 observations in the exterior cusp and cusp/mantle boundary (Figures 4e–4m in Paper 1). In comparison, Figures 7c and 7d show that the outflow ions have a conic pitch-angle distribution with the maximum fluxes peaked around PA = 28°, which is characteristically different pitch-angle distribution from that of the solar wind ions. Such conic pitch-angle distribution is qualitatively similar to what was observed by Cluster C1 within the orange-shaded intervals, hence we explain in Paper 1 that the spacecraft in the cusp and mantle regions likely observed a mixture of the H^+ ions from both the solar wind and the ionosphere.

3.4. Poynting Fluxes and H^+ Outflow in the Lobe After the Shock Impact

To provide an explanation for the processes behind the C3 observations of outflowing ions in the lobe driven by the IP shock presented in Paper 1, we investigate in Figure 8 the simulated outflow driver (downward DC Poynting fluxes) and outflow H^+ ions at location 2 in the lobe (note that the solar wind H^+ ions cannot reach location 2, as shown in Figure 5a). The DC Poynting fluxes $\mathbf{S}_{DC} = \mathbf{E} \times \delta\mathbf{B}_{DC}/\mu_0$, where $\mathbf{E}$ is the electric field and $\delta\mathbf{B}_{DC}$ is magnetic field perturbation for the frequency range of <0.1 Hz. Figure 8a shows that E_y in the lobe is greatly enhanced in response to the shock impact. Figures 8b–8f show the temporal variations of electric drift ($\mathbf{V}_{E\times B}$), $\mathbf{E}$, $\delta\mathbf{B}_{DC}$, field-aligned DC Poynting fluxes ($S_{DC,||}$), and N_{Out} at location 2. Both $\mathbf{E}$ (Figure 8c) and $\delta\mathbf{B}_{DC}$ (Figure 8d) are enhanced from $t \sim 32$ to 40 min, corresponding to the 8 min duration of the IP shock, with the largest changes seen in the E_y and $\delta B_{x,DC}$ components. The increase in $|E_y|$ is a step jump within a minute while the increase in $|\delta B_{x,DC}|$ is gradual. The resulting enhanced $S_{DC,||}$ (Figure 8e) is downward, and the intensity of |

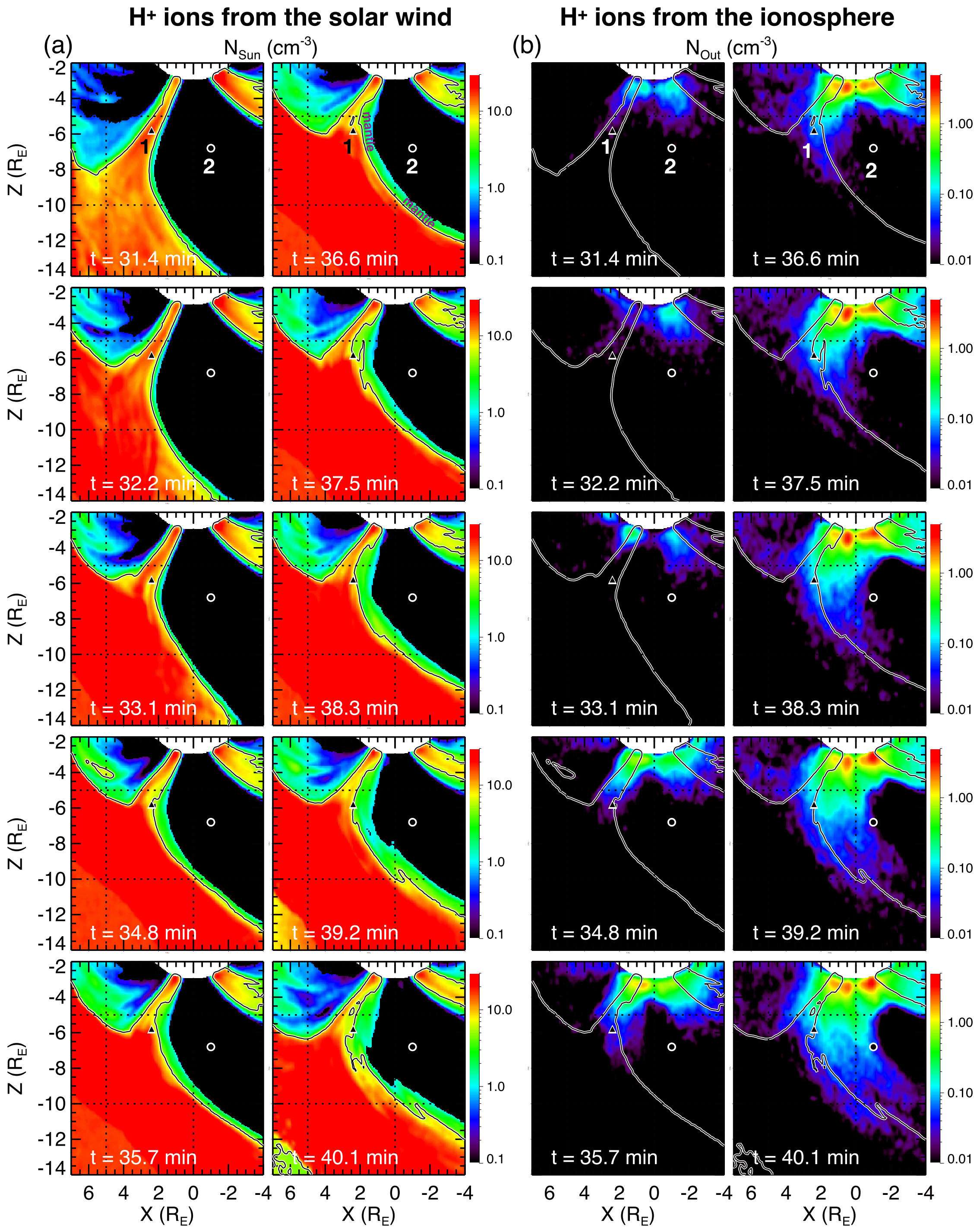

Figure 5. Time sequence of the *X*–*Z* profiles (at $Y = 0$) of the density of the H^+ ions from (a) the solar wind and (b) the ionosphere. The locations 1 and 2 are indicated by the black triangle and black circle, respectively.

$|S_{DC,\parallel}|$ gradually increases from $t \sim 32$ to $t = 39$ min then drops quickly afterward. The enhancements in these field parameters and the resulting outflow driver are qualitatively consistent with the C3 observations shown in Figure 7 of Paper 1. Figure 8f shows that the H^+ density starts to increase at $t \sim 38.5$ min, about 6 min after the increase in downward DC Poynting fluxes. Such time delay between the downward DC Poynting fluxes and the appearance of outflow H^+ ions in the lobe is observed by C3 as shown in Figures 8a and 8b of Paper 1. As can be

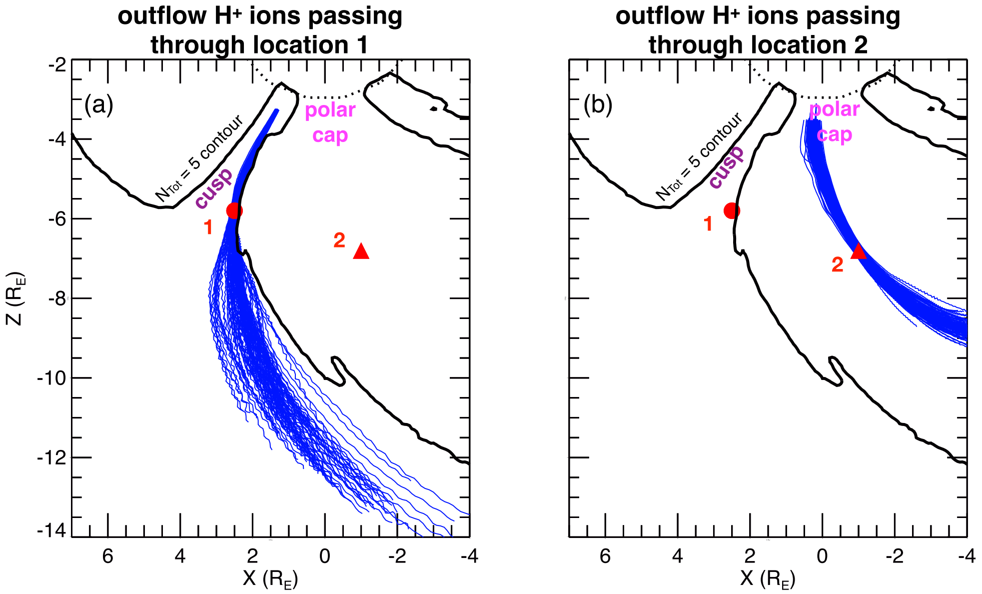

Figure 6. The trajectories for the outflow H^+ ions passing through (a) location 1 and (b) location 2 at $t = 39$ min in the X–Z plane (at $Y = 0$). The black contour is $N_{Tot} = 5$ cm^{-3} at $t = 39.2$ min.

seen in the pitch-angle distributions shown in Figure 8g, the simulated H^+ ions appearing at location 2 have a conic pitch-angle distribution with the peak fluxes at around PA = 28°, which qualitatively resembles the ion conics observed by C3 shown in Figure 5 of Paper 1. Based on the above consistency, we conclude in Paper 1 that the outflowing H^+ ions observed by C3 were plausibly outflow H^+ ions coming from the polar cap.

4. Conclusions and Discussion

We conducted a 3D global hybrid simulation for the impact of an IP shock on the magnetosphere to help us understand an IP shock observation event during which a spacecraft in the southern lobe at altitudes of ~6 R_E observed suprathermal outflowing H^+ ions ~10 min after the shock impact, as reported in Paper 1. We included in the simulation the H^+ ions from both the solar wind source and ionospheric source and investigated the spatial, energy, and pitch-angle distributions for H^+ ions from each source. The solar wind ions have access to the cusp and the mantle, but not to the lobe. Even though there are transient changes in the cusp and mantle locations resulting from the magnetosphere compression by the shock impact and the solar wind ions within these regions can flow upward, the cusp/mantle location is not moving tailward into the lobe and the pitch-angle distribution of the upward-flowing solar wind ions are characteristically different from that of the observed outflowing ions. Thus, the simulation supports our conclusion in Paper 1 that the outflowing ions observed in the lobe were less likely due to the spacecraft encountering the solar wind ions within the moving cusp/mantle. On the other hand, outflow H^+ ions can have access to the lobe as they move upward from the polar cap, in addition to the access to the cusp and mantle. The shock impact enhances downward DC Poynting fluxes, which drives more outflow ions out and flow into these three regions. The time needed for these new outflow H^+ ions to move upward from the polar cap to reach an altitude of ~6 R_E is < 10 min, similar to the observed time delay. Also, these ions at high altitudes have conic pitch-angle distribution, qualitatively resembling that of observed outflowing H^+ ions. Therefore, through this simulation-observation comparison, we conclude that an IP shock can drive a significant amount of suprathermal outflow H^+ ions from the polar cap into the lobe.

As discussed in Paper 1, enhanced downward DC Poynting fluxes can lead to an increase in suprathermal outflows through processes associated with the two scenarios illustrated in Figure 9 of Paper 1. The first is associated with multi-step processes from the F region to topside ionosphere and the second one is associated with the acceleration of pre-existing polar wind ions between ~1,000 and 15,000 km altitudes. In this simulation, we do not explicitly model the processes associated with these two scenarios to generate the suprathermal H^+ ions at the model's inner boundary at $r = 3$. Instead, we specify the outflow parallel and perpendicular temperatures to be

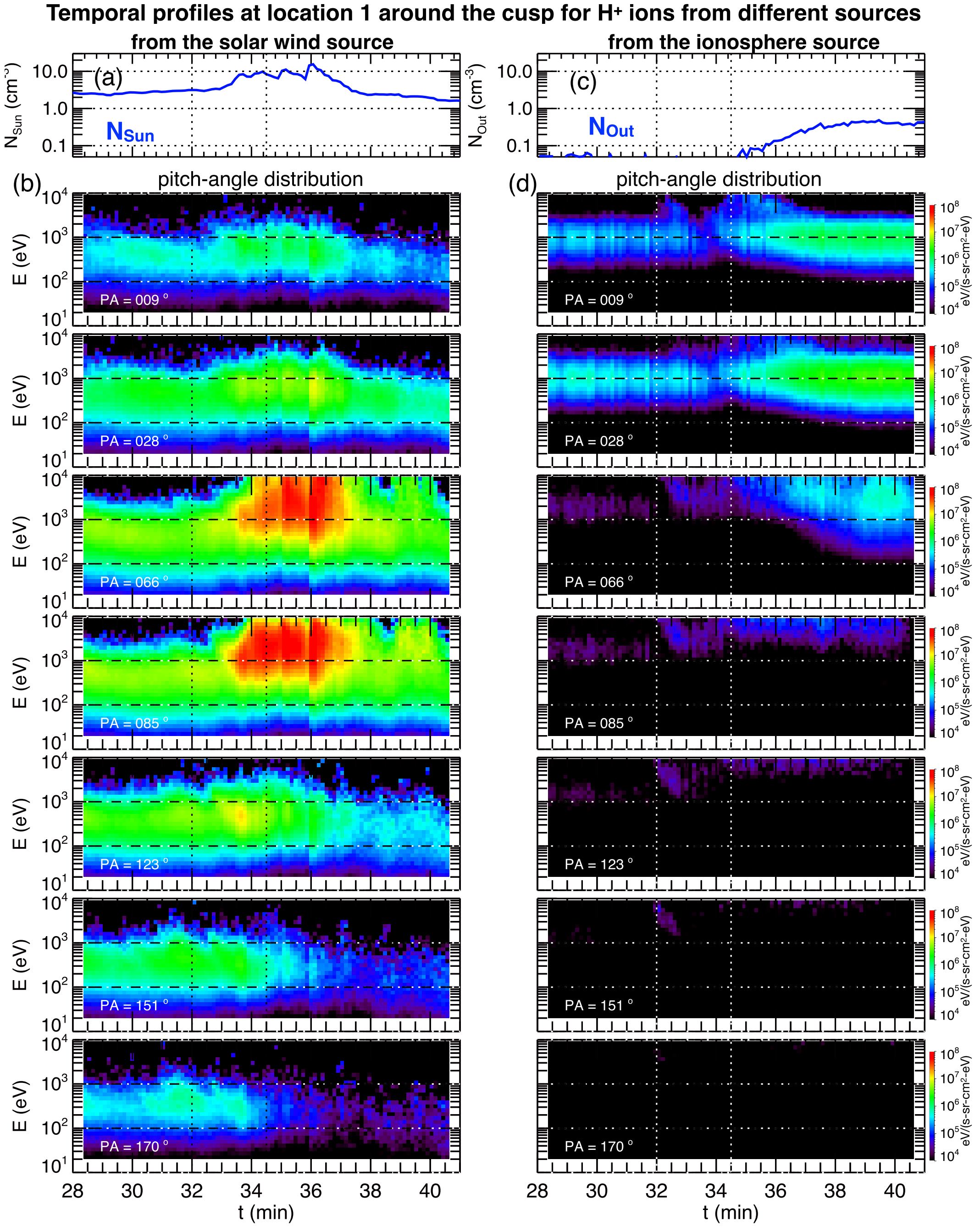

Figure 7. The temporal profiles at location 1 ($X = 2.5$, $Y = 0$, $Z = -5.8\ R_E$, indicated by the triangle in Figure 5a) around the cusp for H^+ ions from the solar wind (left panels) and the ionosphere (right panels). Density for H^+ ions from (a) the solar wind source and (b) ionosphere source. Energy spectrum of energy fluxes at different pitch angles ("PA" is pitch angle) for H^+ ions from (b) the solar wind source and (d) ionosphere source.

100 eV and that there is no time delay between enhanced Poynting fluxes and enhanced outflow fluxes at the inner boundary. This specification approximately describes the suprathermal outflow ions generated in the second scenario. On the other hand, it may take 20–30 min for outflows to be generated in the first scenario. Thus, for the purpose of this simulation to investigate the changes associated with the outflows within the initial 15 min after the shock impact, it is reasonable not to specify the outflow ions corresponding to the first scenario. However, it would be necessary to consider the outflows from both scenarios in a simulation if it is to evaluate the contribution from these outflows over a longer time scale. In addition, our specification of the outflow parallel and

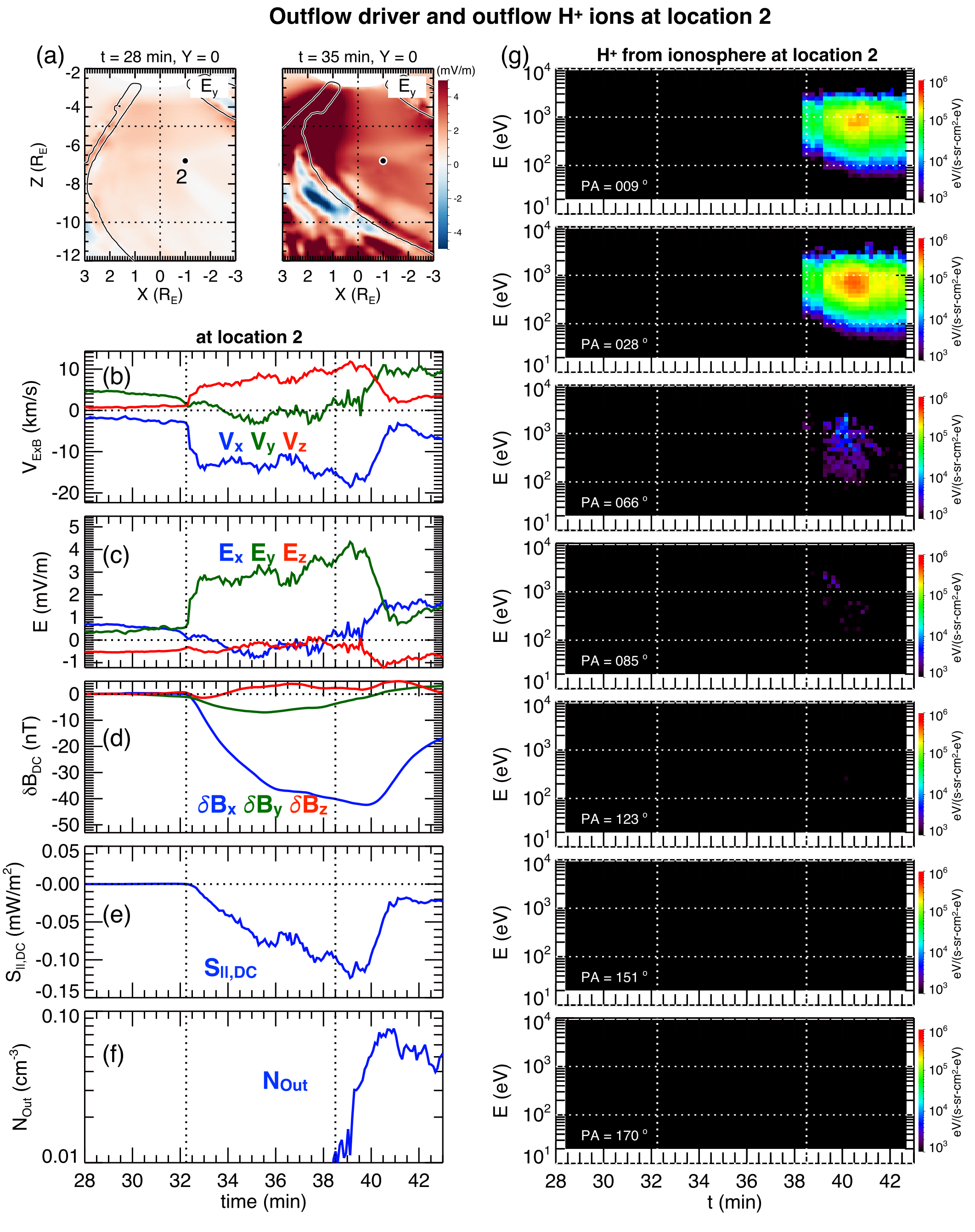

Figure 8. (a) The X–Z profiles ($Y = 0$) of E_y at $t = 28$ (left) and 35 min (right). The temporal profiles at location 2 (indicated by the black circle in (a)) for (b) electric drift, (c) electric fields, (d) DC magnetic field perturbations, (e) field-aligned DC Poynting flux, and (f) density of H^+ ions from the ionosphere. (g) Energy spectrum of energy fluxes at different pitch angles for H^+ ions from the ionosphere at location 2.

perpendicular temperatures to be 100 eV in this run is within a reasonable range based on the travel time from the model inner boundary to location 2 being similar to the observed delay. It is expected that, considering no acceleration or deceleration along the travel path to location 2, the outflow ions corresponding to smaller values of T_{outflow} and $V_{\|,\text{outflow}}$ should have lower energies, thus lower particle speeds, and take longer to reach the lobe location 2. This expectation is confirmed by our test runs with different value ranges, as described in Section 2. For example, Figure S1 in Supporting Information S1 of shows the density for H^+ ions from the ionosphere for one of the test runs using values ($T_{\parallel,\mathrm{outflow}} = T_{\perp,\mathrm{outflow}} = 10$ eV and $V_{\parallel,\mathrm{outflow}} = 2$ km/s) about an order of magnitude smaller than those used in this run. Comparing Figure 5b for this run and Figure S1 in Supporting Information S1 for the test run clearly shows that with smaller T_{outflow} and $V_{\parallel,\mathrm{outflow}}$ values, the outflow ions in the test run move upward more slowly and thus less likely to reach location 2 within the time range that could account for the observed delay. In future studies, more adequate specification of these outflows at a global model's inner boundary can be achieved by coupling it with an outflow model that can physically generate both thermal and suprathermal outflows by considering the multiple processes from the F region up to the topside ionosphere (e.g., Glocer & Daldorff, 2022; Varney et al., 2016b, Varney et al., 2016a).

In our simulation, we relax the restriction of the algorithm of Brambles et al. (2010) to also allow outflows from the polar cap. Only by doing so, we are able to use this simulation to explain the observed outflowing ions in the lobe. We use the empirical formula for the H^+ outflow fluxes in the cusp established by Zhao et al. (2020). The density of the simulated outflow H^+ ions in the lobe is more than an order of magnitude lower than the observed density, indicating that an IP shock is capable of generating significant suprathermal outflow fluxes in the polar cap, as compared to the averages seen in the cusp. These indicate that how to adequately include outflows in the polar-cap region is important in future simulations when evaluating the impact of the ionospheric ions on the magnetosphere during particular solar wind driving conditions, such as an IP shock. For the event we investigated in this paper and Paper 1, the IP shock consisted of large sharp increases in both P_{SW} and solar wind electric field (E_{SW}). It is interesting to determine in future observation or simulation studies whether an increase in P_{SW} or E_{SW} alone can still drive significant outflows from the polar cap.

Data Availability Statement

The simulation data can be found at Wang, Wang, et al. (2024).

Acknowledgments
C.-P. Wang is supported by NASA 80NSSC22K1012 and NSF-GEM 2224108. Xueyi Wang and Yu Lin are supported by NASA 80NSSC22K1012 and NSF-GEM 2224109.

References

Brambles, O. J., Lotko, W., Damiano, P. A., Zhang, B., Wiltberger, M., & Lyon, J. (2010). Effects of causally driven cusp O+ outflow on the storm time magnetosphere-ionosphere system using a multifluid global simulation. *Journal of Geophysical Research*, *115*(A9), A00J04. https://doi.org/10.1029/2010JA015469

Chappell, C. R., Giles, B. L., Moore, T. E., Delcourt, D. C., Craven, P. D., & Chandler, M. O. (2000). The adequacy of the ionospheric source in supplying magnetospheric plasma. *Journal of Atmospheric and Solar-Terrestrial Physics*, *62*(6), 421–436. https://doi.org/10.1016/S1364-6826(00)00021-3

Chappell, C. R., Moore, T. E., & Waite, J. H., Jr. (1987). The ionosphere as a fully adequate source of plasma for the Earth's magnetosphere. *Journal of Geophysical Research*, *92*(A6), 5896–5910. https://doi.org/10.1029/JA092iA06p05896

Glocer, A., & Daldorff, L. K. S. (2022). Connecting energy input with ionospheric upflow and outflow. *Journal of Geophysical Research: Space Physics*, *127*(9), e2022JA030635. https://doi.org/10.1029/2022JA030635

Lin, Y., Wang, X., Sibeck, D. G., Wang, C.-P., & Lee, S.-H. (2022). Global asymmetries of hot flow anomalies. *Geophysical Research Letters*, *49*(4), e2021GL096970. https://doi.org/10.1029/2021GL096970

Lin, Y., Wang, X. Y., Lu, S., Perez, J. D., & Lu, Q. (2014). Investigation of storm time magnetotail and ion injection using three-dimensional global hybrid simulation. *Journal of Geophysical Research: Space Physics*, *119*(9), 7413–7432. https://doi.org/10.1002/2014JA020005

Omidi, N., Blanco-Cano, X., Russell, C. T., & Karimabadi, H. (2006). Dipolar magnetospheres and their characterization as a function of magnetic moment. *Advances in Space Research*, *33*(11), 1996–2003. https://doi.org/10.1016/j.asr.2003.08.041

Peterson, W. K., Andersson, L., Callahan, B. C., Collin, H. L., Scudder, J. D., & Yau, A. W. (2008). Solar-minimum quiet time ion energization and outflow in dynamic boundary related coordinates. *Journal of Geophysical Research*, *113*(A7), A07222. https://doi.org/10.1029/2008JA013059

Strangeway, R. J., Ergun, R. E., Su, Y.-J., Carlson, C. W., & Elphic, R. C. (2005). Factors controlling ionospheric outflows as observed at intermediate altitude. *Journal of Geophysical Research*, *110*(A3), A03221. https://doi.org/10.1029/2004JA010829

Varney, R., Wiltberger, M., Zhang, B., Lotko, W., & Lyon, J. (2016a). Influence of ion outflow in coupled geospace simulations: 2. Sawtooth oscillations driven by physics-based ion outflow. *Journal of Geophysical Research: Space Physics*, *121*(10), 9688–9700. https://doi.org/10.1002/2016JA022778

Varney, R. H., Wiltberger, M., Zhang, B., Lotko, W., & Lyon, J. (2016b). Influence of ion outflow in coupled geospace simula-tions: 1. Physics-Based ion outflow model development and sen-sitivity study. *Journal of Geophysical Research: Space Physics*, *121*(10), 9671–9687. https://doi.org/10.1002/2016JA022777

Wang, C.-P., Mouikis, C. G., Wang, X., Masson, A., & Lin, Y. (2024). Suprathermal outflowing H^+ ions in the lobe driven by an interplanetary shock: 1. An observation event. *Journal of Geophysical Research: Space Physics*, *129*, e2024JA032557. https://doi.org/10.1029/2024JA032557

Wang, C.-P., Wang, X., & Lin, Y. (2023). Transport and acceleration of O^+ ions in upstream solar wind due to impact of an IMF discontinuity: 3D global hybrid simulation. *Geophysical Research Letters*, *50*(15), e2023GL103883. https://doi.org/10.1029/2023GL103883

Wang, C.-P., Wang, X., Lin, Y., Mouikis, C. G., & Masson, A. (2024). Dataset of suprathermal outflowing H^+ ions in the lobe driven by an interplanetary shock: 2. A 3D global hybrid simulation [Dataset]. *Zenodo*. https://doi.org/10.5281/zenodo.10625471

Wang, C.-P., Wang, X., Liu, T. Z., & Lin, Y. (2020). Evolution of a foreshock bubble in the midtail foreshock and impact on the magnetopause: 3-D global hybrid simulation. *Geophysical Research Letters*, *47*(22), e2020GL089844. https://doi.org/10.1029/2020GL089844

Wang, C.-P., Wang, X., Liu, T. Z., & Lin, Y. (2021a). A foreshock bubble driven by an IMF tangential discontinuity: 3D global hybrid simulation. *Geophysical Research Letters*, *48*(9), e2021GL093068. https://doi.org/10.1029/2021GL093068

Wang, C.-P., Wang, X., Liu, T. Z., & Lin, Y. (2021b). Impact of foreshock transients on the flank magnetopause and magnetosphere and the ionosphere. *Frontiers in Astronomy and Space Sciences*, *8*, 160. https://doi.org/10.3389/fspas.2021.751244

Wang, C.-P., Xing, X., Wang, X., Avanov, L. A., Lin, Y., Strangeway, R. J., & Wei, H. Y. (2022). Effect of IMF b*y* on the entry of solar wind ions into the near-Earth tail lobe: Global hybrid simulation and MMS observation. *Journal of Geophysical Research: Space Physics*, *127*(9), e2022JA030800. https://doi.org/10.1029/2022JA030800

Yau, A., Peterson, W., & Abe, T. (2011). Influences of the ionosphere, thermosphere and magnetosphere on ion outflows. *The Dynamic Magnetosphere*, 283–314. https://doi.org/10.1007/978-94-007-0501-2_16

Zhao, K., Kistler, L. M., Lund, E. J., Nowrouzi, N., Kitamura, N., & Strangeway, R. J. (2020). Factors controlling O^+ and H^+ outflow in the cusp during a geomagnetic storm: FAST/TEAMS observations. *Geophysical Research Letters*, *46*(11), e2020GL086975. https://doi.org/10.1029/2020GL086975